BRAIN
ORIGINAL ARTICLE

SREBP2 gene therapy targeting striatal astrocytes ameliorates Huntington's disease phenotypes

Giulia Birolini,[1,2] Gianluca Verlengia,[3,4] Francesca Talpo,[5] Claudia Maniezzi,[5] Lorena Zentilin,[6] Mauro Giacca,[6,7] Paola Conforti,[1,2] Chiara Cordiglieri,[2] Claudio Caccia,[8] Valerio Leoni,[9,10] (iD)Franco Taroni,[8] Gerardo Biella,[5] (iD)Michele Simonato,[3,4] Elena Cattaneo[1,2] and Marta Valenza[1,2]

Brain cholesterol is produced mainly by astrocytes and is important for neuronal function. Its biosynthesis is severely reduced in mouse models of Huntington's disease. One possible mechanism is a diminished nuclear translocation of the transcription factor sterol regulatory element-binding protein 2 (SREBP2) and, consequently, reduced activation of SREBP2-controlled genes in the cholesterol biosynthesis pathway.

Here we evaluated the efficacy of a gene therapy based on the unilateral intra-striatal injection of a recombinant adeno-associated virus 2/5 (AAV2/5) targeting astrocytes specifically and carrying the transcriptionally active N-terminal fragment of human SREBP2 (hSREBP2).

Robust hSREBP2 expression in striatal glial cells in R6/2 Huntington's disease mice activated the transcription of cholesterol biosynthesis pathway genes, restored synaptic transmission, reversed dopamine receptor D2 (*Drd2*) transcript levels decline, cleared mutant huntingtin aggregates and attenuated behavioural deficits. We conclude that glial SREBP2 participates in Huntington's disease brain pathogenesis *in vivo* and that AAV-based delivery of SREBP2 to astrocytes counteracts key features of the disease.

1 Department of Biosciences, University of Milan, 20133, Milan, Italy
2 Istituto Nazionale di Genetica Molecolare "Romeo ed Enrica Invernizzi", 20122, Milan, Italy
3 Division of Neuroscience, IRCCS San Raffaele Hospital, 20132, Milan, Italy
4 Department of BioMedical Sciences, Section of Pharmacology, University of Ferrara, 44121, Ferrara, Italy
5 Department of Biology and Biotechnologies, University of Pavia, 27100, Pavia, Italy
6 International Centre for Genetic Engineering and Biotechnology, ICGEB, 34149, Trieste, Italy
7 School of Cardiovascular Medicine and Sciences, King's College London, SE5 9NU, UK
8 Unit of Medical Genetics and Neurogenetics. Fondazione IRCCS Istituto Neurologico Carlo Besta, 20131 Milan, Italy
9 School of Medicine and Surgery, University of Milano-Bicocca, 20900, Monza, Italy
10 Laboratory of Clinical Pathology, Hospital of Desio, ASST Monza, 20900, Monza, Italy

Correspondence to: Marta Valenza
Department of Biosciences, University of Milan, and Istituto Nazionale di Genetica Molecolare
"Romeo ed Enrica Invernizzi", via F. Sforza 35, 20122, Milan, Italy
E-mail: marta.valenza@unimi.it

Abbreviations: 24S-OHC = 24S-hydroxycholesterol; AAV = adeno-associated virus; m/sEPSCs = miniature/spontaneous excitatory postsynaptic currents; m/sIPSCs = miniature/spontaneous inhibitory postsynaptic currents; MSNs = medium-sized spiny neurons; muHTT = mutant HTT

Introduction

Cholesterol is a multifaceted molecule that plays key roles in the brain during development and in adulthood. Its concentration in the brain is higher than in any other tissue (15–20 mg/g tissue).[1] Up to 70–80% of cholesterol in the adult brain is present in myelin sheaths, while the rest is localized in the plasma membranes of astrocytes and neurons.[2] In neurons cholesterol plays important roles in synaptic transmission, as it is required for synaptic vesicle formation and function[3–5] and for optimal neurotransmitter release.[6–8] As the blood–brain barrier efficiently prevents the passage of circulating cholesterol, brain cholesterol is synthesized locally.[9] Of note, in adulthood astrocytes are believed to synthetize most cholesterol, which is transferred to the neurons via APOE-containing lipoproteins.[3,10]

Cholesterol biosynthesis is regulated by sterol regulatory element-binding protein 2 (SREBP2), the transcription factor that activates the expression of most cholesterol biosynthesis genes. When the cells need to produce cholesterol, SREBP2, which is localized as an inactive form at the membrane of the endoplasmic reticulum, is translocated to the Golgi apparatus by the SREBP cleavage activation protein (SCAP). SREBP2 is then cleaved by two proteases called site 1 (S1P) and site 2 (S2P) proteases, resulting in a N-terminal active fragment moving towards the nucleus, binds the sterol response element (SRE) in the promoters of target genes, and activates their transcription.[11,12]

Dysregulation of brain cholesterol homeostasis has been linked to several neurodegenerative diseases.[13,14] Among these conditions is Huntington's disease, an adult-onset disorder characterized by motor, cognitive and psychiatric features. Huntington's disease is caused by a CAG expansion in the *HTT* gene (previously known as *IT15*), which encodes the huntingtin (HTT) protein, and it is characterized by progressive loss of striatal medium-sized spiny neurons (MSNs) and cortical pyramidal neurons.[15,16]

A large number of studies conducted in different Huntington's disease rodent models have demonstrated significantly reduced biosynthesis of cholesterol in the brain, with the striatum being affected first.[17–21] In the adult Huntington's disease mouse brain, this dysfunction is evidenced by a decreased level of cholesterol precursors and by a reduced rate of *de novo* cholesterol biosynthesis, it precedes the onset of motor symptoms, is CAG-dependent—as confirmed by studies in an allelic series of Huntington's disease mice—and it leads to a reduced content of total cholesterol at late symptomatic stages.[21] The nuclear level and activity of the N-terminal active fragment of SREBP2 are reduced in Huntington's disease cellular models and mouse brains,[17,22] probably through sequestration in the cytoplasm of the SREBP2/importin β complex required for nuclear import.[23] Astrocytes are central in this dysfunction, as highlighted by *in vitro* studies. In fact, *SREBP2* gene silencing in wild-type astrocytes has detrimental effects on Huntington's disease neurons,[22] while the forced expression of the N-terminal active fragment of SREBP2 in Huntington's disease astrocytes reverses neurite outgrowth and synaptic defects in Huntington's disease neurons,[22] suggesting that active SREBP2 might be a candidate target for *in vivo* approaches.

To gain mechanistic insights and confidence in the biological relevance of targeting this pathway *in vivo*, we forced the expression of the N-terminal active fragment of human SREBP2 (hSREBP2) in striatal astrocytes of the R6/2 transgenic mouse model of Huntington's disease by using a recombinant adeno-associated virus 2/5 (AAV2/5). We found that increasing hSREBP2 level specifically in the nucleus of astrocytes stimulates cholesterol biosynthesis in the striatum of R6/2 mice. As a consequence, synaptic transmission of both inhibitory and excitatory synapses is restored, the number of striatal MSNs expressing dopamine receptor D2 (Drd2) receptors normalized, mutant HTT (muHTT) aggregation reduced, motor defects ameliorated and cognitive decline is completely rescued.

Materials and methods

Colony management

Our R6/2 colony lifespan was ∼13 weeks and it was maintained through the male line exclusively.[24] Transgenic R6/2 males were paired with non-carrier females (B6CBA-Tg(HDexon1)62Gpb/1J, stock n. 002810, purchased from Charles River). The CAG repeat length of the animals used in this study was 150–180 CAGs (Laragen). Changes that could affect strain productivity, general behaviour, litter size, pup survival, genotype frequency and phenotype were constantly monitored.

The Drd2-eGFP colony is a transgenic mouse line generated in 2003 by the Gene Expression Nervous System Atlas project at Rockefeller University in New York.[25] Primary labelling was found to occur in Drd2-positive MSNs from the indirect basal ganglia pathway. In this work, this model was crossed with R6/2 mice to label *in vivo* Drd2-expressing MSNs.

All mice were weaned at 21 days (±3 days). Mice were housed under standard conditions (22 ± 1°C, 60% relative humidity, 12-h light/dark cycle, three to four mice per cage, with food and water provided *ad libitum*). After PCR genotyping,[24,25] male and female mice were included and randomly divided into experimental groups. Littermates were included as controls.

Animal care was conducted in accordance with standard ethical guidelines approved by the Italian Governing Law (D.lgs 26/2014; Authorization no. 324/2015-PR issued 6 May, 2015 by Ministry of Health); the NIH Guide for the Care and Use of Laboratory Animals (2011 edition) and the EU directives and guidelines (EEC Council Directive 2010/63/UE) and the local ethics committee approved the experiments.

Vector production

We obtained the AAV vector plasmid pZac-gfaABC1D-hSREBP2-tdTomato, expressing the N-terminal active fragment of hSREBP2 [1–402 amino acids (aa)] fused with tdTomato, starting from pZac2.1 gfaABC1D-tdTomato (from Addgene) and pcDNA3.1 hSREBP2(402)-eGFP (from T. Osborne).[26] During cloning, a stop codon was accidentally inserted immediately after the *hSrebp2* sequence. This codon caused a frameshift in the *tdTomato* sequence and prevented its translation. In the AAV vector plasmids, the transgenes are under the control of the minimal *GFAP* promoter

(gfaABC1D) and are surrounded by the inverted terminal repeats derived from AAV serotype 2.

These plasmids were used to generate the corresponding AAV vectors in the AAV Vector Unit at the International Centre for Genetic Engineering and Biotechnology Trieste (http://www.icgeb.org/avu-core-facility.html), as described previously[27] with few modifications. Briefly, infectious recombinant AAV vector particles were generated in human embryonic kidney 293T cells culture in roller bottles by a cross-packaging approach, whereby the vector genome was packaged into AAV capsid serotype-5. Viral stocks were obtained by PEG precipitation and $CsCl_2$ gradient centrifugation.[28] The physical titre of recombinant AAVs was determined by quantifying vector genomes packaged into viral particles by quantitative PCR (qPCR) against a standard curve of a plasmid containing the vector genome.[29] Values obtained were 1.7×10^{14} and 1.7×10^{13} gc/ml for AAV2/5-gfaABC1D-tdTomato and AAV2/5-gfaABC1D-hSREBP2, respectively.

HSV1/JDNI8-gfaABC1D-tdTomato $(5 \times 10^9 \, \text{pfu/ml})$ was produced and purified as previously described.[30] Briefly, ICP4/ICP27-complementing U2OS cells were transfected with a purified BAC-DNA engineered to contain the HSV1-JDNI8/gfaABC1D-tdTomato vector genome. Then, 10 days after transfection, the virus-containing supernatant was collected and used for subsequent infections of ICP4/ICP27-U2OS complementing cells to obtain a highly concentrated monoclonal vector stock suitable for *in vivo* applications. Estimation of HSV1 vector titres was carried out by qPCR quantification of glycoprotein D gene copy number.[30]

Stereotaxic injection of viral vectors

Seven-week-old mice were deeply anaesthetized with Avertin 2.5% (15 μl/g body weight). The virus was injected unilaterally by implantation of a borosilicate glass needle into the right striatum of mice via stereotaxic surgery using an automated infusion syringe pump (KD Scientific, KDS100), on which a 50 μl Gastight Syringe Model 1705 TLL with PTFE Luer Lock (Hamilton, 80920) could be mounted. To favour needle entry and vector spread in the injected striata, we used borosilicate needles customized by laser shaping with the Leica Laser Microdissector CTR6000 (Leica Microsystems), that allowed a 45° edge chamfering of tip (inner diameter at tip = 60 μm) and, moreover, to open an additional circular hole (diameter 20 μm) about 100 μm from the bevelled edge.[31]

The following stereotaxic coordinates were used: 2 mm lateral to midline, 0.74 mm rostral to the bregma and 3.5 mm ventral to the skull surface.[32] The rate of injection was 12 μl/h with a total volume of 2 μl.

Assessment of post-operative pain and distress was performed using a specific table for pain scoring based on behavioural indicators of well-being and monitoring mouse body weight.[33]

Immunohistochemistry analysis

Four weeks after the infection, anaesthetized mice were transcardially perfused with paraformaldehyde (PFA) 4%. Brains were postfixed overnight in PFA 4% at 4°C and then in 30% sucrose to prevent ice crystal damage during freezing in optimal cutting temperature (OCT) medium.

Next, 15 μm or 30 μm coronal sections were prepared for immunohistochemical analysis. Epitopes were demasked at 98°C with sodium citrate 10 mM for 15 min and then slices were incubated with the following primary antibodies for 3 h at room temperature: mouse anti-SREBP2 (1:100; LSBio, LS-C179708), rabbit anti-SREBP2 (1:100; LSBio, LS-B4695), rabbit anti-RFP (1:100, MBL, PM005), mouse anti-RFP (1:100, Thermo Fisher, MA5-15257), rabbit anti-DARPP32

(1:100; Cell Signaling, 2306), mouse anti-NeuN (1:100; Millipore, MAB377); rabbit anti-GFAP (1:250; Dako, Z0334), rabbit anti-IBA1 (1:100, Wako, 019–19741), rabbit anti-S100B (1:100; Sigma Aldrich, S2644); mouse anti-HTT clone EM48 (1:100; Millipore, MAB5374) and mouse anti-HTT clone 1HU-4C8 (1:100; Millipore, MAB2166). Anti-rabbit Alexa Fluor® 568-conjugated goat secondary antibodies (1:500; Invitrogen), anti-rabbit Alexa Fluor® 633-conjugated goat secondary antibodies (1:500; Invitrogen) or anti-mouse Alexa Fluor® 488-conjugated goat secondary antibodies (1:500; Invitrogen) were used for detection (1 h at room temperature). Sections were counterstained with the nuclear dye Hoechst 33258 (1:10.000, Invitrogen) and then mounted under coverslips using Vectashield (Vector Laboratories).

Image acquisition and quantification

Confocal images (5–10 z-steps) were acquired with a LEICA SP5 laser scanning confocal microscope at ×40 magnification [numerical aperture (NA) 1.40]. Laser intensity and detector gain were maintained constant for all images within the same set of experiments. Stitched images were acquired at ×4 magnification (NA 0.75) with a customized Nikon Ti microscope, equipped with a X-light V2 spinning-disc scan head with VCS module for structure illumination (Crest Optics).

For a subset of confocal images (n = 7–8/group), to quantify the number of cells, the nuclei and the positive cells for each cellular marker and for tdTomato were counted by using the Cell Counter plugin of ImageJ (on the Fiji platform). To distinguish between ramified and amoeboid IBA1$^+$ cells, we designed *ad hoc* a specific pipeline of image analysis using NIS-Elements v.5.30, with complex object segmentation, classification and quantification, based on different binary thresholding of the IBA1$^+$ signal, implying cell-range filtering, based on shape parameters, such as object circularity and elongation. To quantify the amount of SREBP2 inside the nucleus, confocal images (n = 7–8/group) were segmented using NIS-Elements v.5.30. A threshold was applied to both channels and the intensity ratio of SREBP2/Hoechst was measured. To quantify the number and the size of aggregates, 18 confocal images/mouse from nine sections throughout the entire striatum were analysed. ImageJ software (on the Fiji platform) was used to measure the fluorescence signal. Images were split into three colour channels and the same global threshold was set on each signal histogram. To count the number of aggregates in the nucleus of DARPP32, NeuN, S100B or GFAP-positive cells, NIS-Elements v.5.30 was used. To evaluate co-localization between SREBP2 and muHTT, images were analysed with Analyse Plot plugin of ImageJ (on the Fiji platform).

RNA extraction, reverse transcription and quantitative PCR

Four weeks after the infection, mice were euthanized by cervical dislocation and tissues were isolated and frozen. Total RNA from the infused striatum and the ipsilateral cortex of treated mice was extracted with TRIzol® reagent (Life Technologies, 15596026). RNA quality check was carried out on 1% agarose gel. Potential contamination of DNA was removed using the Ambion® DNA-free™ Kit (Invitrogen, AM1906). Then 500 ng of RNA was retrotranscribed to single-stranded cDNA using the iScript cDNA synthesis kit (Bio-Rad, 1708891). The analyses were performed in batches of three animals per group. For each sample, two different reverse transcriptions (RT) were performed. For each cDNA reaction, one or two conventional qPCRs were performed in a CFX96 Real-Time System (Bio-Rad) in a 15 μl volume containing diluted cDNA and 7.5 μl iQ EVA Green Supermix (Bio-Rad, 172–5204), 7.5 μl nuclease-free water and 0.33 μM forward and reverse primers. The amounts

of target transcript were normalized to β-actin as reference gene. Supplementary Table 1 summarizes the primer sequences and melting temperature used in this work.

Mass spectrometry analysis

To a screw-capped vial sealed with a Teflon-lined septum were added the following: 50 µl of homogenates together with 500 ng of D4-lathosterol (CDN Isotopes), 500 ng of D6-desmosterol (Avantipolar Lipids), 100 ng of D6-lanosterol (Avantipolar Lipids), 400 ng of D7-24S-hydroxycholesterol (25S-OHC) (Avantipolar Lipids) and 100 µg of epicoprostanol (Sigma-Merck) as internal standards, 50 µl of butylated hydroxytoluene (BHT) (5 g/l) and 25 µl of EDTA (10 g/l). Argon was flushed through to remove air. Alkaline hydrolysis was allowed to proceed at room temperature (22°C) for 1 h in the presence of 1 M ethanolic potassium hydroxide solution under magnetic stirring. After hydrolysis, the neutral sterols (cholesterol, lathosterol, desmosterol and lanosterol) and 24S-OHC were extracted twice with 5 ml of hexane. The organic solvents were evaporated under a gentle stream of nitrogen and converted into trimethylsilyl ethers with BSTFA-1% TMCS (Cerilliant) at 70°C for 60 min. Analysis was performed by gas chromatography–mass spectrometry (GC–MS) on a Clarus 600 gas chromatograph (Perkin Elmer) equipped with Elite-5MS capillary column (30 m, 0.32 mm, 0.25 µm. Perkin Elmer) connected to Clarus 600C mass spectrometer (Perkin Elmer). The oven temperature programme was as follows: the initial temperature 180°C was held for 1 min, followed by a linear ramp of 20°C/min to 270°C and then a linear ramp of 5°C/min to 290°C, which was held for 10 min. Helium was used as carrier gas at a flow rate of 1 ml/min and 1 µl of sample was injected in splitless mode. Mass spectrometric data were acquired in selected ion monitoring mode. Peak integration was performed manually. Sterols and 24S-OHC were quantified against internal standards, using standard curves for the listed sterols.[34]

Synaptosomes preparation and western blot analysis

Mice were euthanized by cervical dislocation and the tissues were isolated and frozen. Syn-PER™ Synaptic Protein Extraction Reagent (Thermo Fisher Scientific, 87793) was used for synaptosome purification from the infused striatum and the ipsilateral cortex accordingly to the manufacturer instruction. Briefly, a volume of 10 ml of Syn-PER™ Reagent per gram of tissue was added and tissues were homogenized on ice. The homogenate was centrifuged at 1200*g* for 10 min at 4°C. The supernatant was centrifuged at 15 000*g* for 20 min at 4°C to pellet synaptosomes. The pellet was resuspended in Syn-PER™ Reagent. Proteins were quantified with Pierce™ BCA Protein Assay Kit (Thermo Fisher Scientific, 23225).

Equal amounts of protein (15–20 µg) were separated by SDS-PAGE using Criterion TGX Stain Free Precast Gels 7.5% (Bio-Rad, 5678023) or Any kD™ (Bio-Rad, 5678123) gels for detection of synaptic proteins and SREBP2, and Criterion XT Precast Gels 3–8% Tris-Acetate (Bio-Rad, 3450129) gels for detection of SDS-insoluble muHTT (muHTT aggregates). Proteins were transferred to nitrocellulose using the TransBlot Turbo apparatus (Bio-Rad). Membranes were blocked in 5% milk in Tris-buffered saline and polysorbate 20 (Tween 20) at room temperature, then incubated in the following antibodies overnight at 4°C: rabbit anti-RFP (1:1000; MBL, PM005), rabbit anti-SREBP2 (1:1000; LSBio, LS-B4695), mouse anti-SYP (1:500; Abcam, ab8049), mouse anti-SNAP25 (1:1000; Abcam, ab66066), rabbit anti-VAMP1 (1:1000; Abcam, ab151712), mouse anti-PSD95 (1:1000; SySy, 124011), rabbit anti-SHANK3 (1:1000; SySy, 162302), rabbit anti-NMDAR1 (1:500; MerckMillipore, Ab9864),

rabbit anti-GAPDH (1:5000; Abcam, ab37168), mouse anti-Huntingtin clone EM48 (1:1000; Millipore, MAB5374) and rabbit anti-calnexin (1:5000; Invitrogen, PA5-34754). Goat anti-mouse IgG-HRP (1:3000; Bio-Rad, 1706516) or Goat anti-rabbit IgG-HRP (1:3000; Bio-Rad, 1706515) were used for detection (1 h at room temperature). Bands were detected using Clarity™ Western ECL Substrate (Bio-Rad, 1705061) or SuperSignal™ West Femto Maximum Sensitivity Substrate (Thermo Fisher Scientific, 34096) using the ChemiDoc MP System (Bio-Rad). GAPDH, calnexin or six different protein bands of the stain-free technology were used as loading control and reference for protein normalization. Four animals per group were analysed by western blotting and two or three technical replicates were performed for each protein.

X-CLARITY™ processing and 2-photon imaging of cleared tissues

R6/2 mice were crossed with mice that had Drd2-expressing MSNs tagged with GFP to obtain a line with GFP-MSNs neurons from the indirect pathway. At 7 weeks of age, Drd2-wild-type (Drd2-wt) mice were infected with AAV2/5-gfaABC1D-tdTomato (Drd2-wt-Tom) while Drd2-R6/2 mice were infected with AAV2/5-gfaABC1D-tdTomato (Drd2-R6/2-Tom) or with AAV2/5-gfaABC1D-hSREBP2 (Drd2-R6/2-hBP2). Then 4 weeks after the infection, anaesthetized mice were transcardially perfused with PFA 4%. Brains were post-fixed overnight and sliced with a Leica VT1000S Vibrating blade microtome (Leica Biosystems). From each mouse, two 1-mm thick coronal brain slices were prepared, from which the infused and the contralateral striatum were isolated. Tissues were clarified using the X-CLARITY™ system (Logos Biosystem) according to manufacturer instructions. Briefly, tissues were incubated in embedding solution (Logos Biosystems, C13104) at 4°C for 24 h at most, allowing hydrogel monomers to diffuse uniformly throughout the samples and to covalently link biomolecules including proteins, nucleic acids and small molecules. Polymerization was performed by placing the samples within the X-CLARITY Polymerization at 37°C for 3 h under vacuum condition (–90 kPa). Following washing steps, the hydrogel-embedded tissues were rinsed with electrophoretic tissue clearing (ETC) Solution (Logos Biosystems, C13001) and moved into the X-CLARITY™ Tissue Clearing System II (Logos Biosystems, C30001) chamber, filled with the ETC solution in which the application of a uniform electric current (1.5 A) at a controlled temperature of 37°C enabled the active extraction of lipids from tissues in about 2–3 h.

After clearing, samples were washed with PBS 1× overnight at room temperature to remove residual SDS. The endogenous signal [enhanced green fluorescent protein (eGFP)] was acquired by using a A1 MP+ microscope (Nikon) equipped with Ti:sapphire MP tuneable laser (680–1080 nm) using the water plan-Apo LWD ×25 objective (NA 1.1). Images were acquired with the following settings: 16 bit, z-stack of ∼400 µm with a z-step size of 5 µm. The endogenous fluorescent protein eGFP was excited at a wavelength of 900 nm. For each striatum, 2–3 images were acquired. Images were processed using NIS-Elements AR software v.5.21(Nikon-Lim). First, a 3D deconvolution Richardson–Lucy algorithm was applied to improve image quality. Afterwards, the background was removed using the rolling ball correction. To quantify the number of cells expressing eGFP, a segmentation 3D-object mask was applied over the 3D-reconstructed volume, using a specialized algorithm package in NIS-Elements AR v.5.21. For each image, the number of cells expressing eGFP was normalized on the z-volume acquired.

Electrophysiological analysis

Experiments were performed on submerged brain slices obtained from 12-week-old mice. Animals were anaesthetized by inhalation of isoflurane and decapitated. The head was rapidly submerged in ice-cold (∼4°C) and oxygenated (95% O_2–5% CO_2) cutting solution containing: sucrose 70 mM, NaCl 80 mM, KCl 2.5 mM, $NaHCO_3$ 26 mM, glucose 15 mM, $MgCl_2$ 7 mM, $CaCl_2$ 1 mM and NaH_2PO_4 1.25 mM. Striatal coronal slices (300-µm thick) were cut using a vibratome (DTK-1000, Dosaka EM) and allowed to equilibrate for at least 1 h in a chamber filled with oxygenated artificial CSF containing: NaCl 125 mM, KCl 2.5 mM, $NaHCO_3$ 26 mM, glucose 15 mM, $MgCl_2$ 1.3 mM, $CaCl_2$ 2.3 mM and NaH_2PO_4 1.25 mM. The slices collected from the hemisphere ipsilateral to the infusion site were transferred to a submerged-style recording chamber at room temperature (∼23–25°C) and were continuously perfused at 1.4 ml/min with artificial CSF. The chamber was mounted on an E600FN microscope (Nikon) equipped with ×4 and ×40 water-immersion objectives (Nikon) and connected to a near-infrared CCD camera for cells visualization.

Data were obtained from MSNs using the whole-cell patch-clamp technique in both voltage- and current-clamp mode. The patch pipette was produced from borosilicate glass capillary tubes (Hilgenberg GmbH) using a horizontal puller (P-97, Sutter instruments) and filled with an intracellular solution containing: Cs-methanesulphonate 120 mM, KCl 5 mM, $CaCl_2$ 1 mM, $MgCl_2$ 2 mM, EGTA 10 mM, Na_2ATP 4 mM, Na_3GTP 0.3 mM, HEPES 8 mM and lidocaine N-ethylbromide 5 mM (added to inhibit firing by blocking intracellularly the voltage-sensitive Na^+ channels) (pH adjusted to 7.3 with KOH). Spontaneous excitatory postsynaptic currents (sEPSCs), mediated by the activation of ionotropic glutamate receptors, were recorded from MSNs at a holding potential of –70 mV, whereas spontaneous inhibitory postsynaptic currents (sIPSCs), elicited by the activation of $GABA_A$ receptors, were assessed at a holding potential of 0 mV. Miniature excitatory (mEPSCs) and inhibitory (mIPSCs) events were recorded in presence of the Na^+ channel blocker tetrodotoxin (TTX) 1 µM. The signals were amplified with a MultiClamp 700B amplifier (Molecular Devices) and digitized with a Digidata 1322 computer interface (Digitata, Axon Instruments Molecular Devices). Data were acquired using the software Clampex 9.2 (Molecular Devices), sampled at 20 kHz and filtered at 2 kHz.

The off-line detection of spontaneous postsynaptic currents (sPSCs) was performed manually using a custom-made software in Labview (National Instruments). The amplitudes of sPSCs obeyed a log-normal distribution. Accordingly, the mean amplitude was computed as the peak of the log-normal function used to fit the distribution. Intervals (measured as time between two consecutive sPSCs) for spontaneous events were distributed exponentially and the mean interval was computed as the tau ($\tau_{interval}$) value of the mono-exponential function that best fitted this distribution. The reciprocal of τ ($1/\tau$) is the mean of the instantaneous frequencies of sPSCs. Furthermore, the analysis of the membrane capacitance (C_m) and the input resistance (R_{in}) was performed using Clampfit 10.2 (Molecular Devices). C_m was estimated from the capacitive current evoked by a –10 mV pulse, whereas R_{in} was calculated from the linear portion of the IV relationship obtained by measuring steady-state voltage responses to hyperpolarizing and depolarizing current steps.

Behavioural tests

Mice behaviour was evaluated at 11 weeks of age. Animals were assigned randomly and sex was balanced in the various experimental groups. All the behavioural analyses were performed blind.

Activity cage

Spontaneous locomotor activity was evaluated by the activity cage test, in presence of a low-intensity white light source. The animal was placed in the centre of the testing, transparent, arena (25 × 25 cm) (2Biological Instrument) and allowed to freely move for 1 h. Following 15 min of habituation, both horizontal and vertical motor activities were assessed by an automated tracking system (Actitrack software, 2Biological Instrument) connected to infrared sensors surrounding the arena. Total distance travelled, mean velocity speed, stereotyped movements and numbers of rearings were evaluated. The percentage of time that mice explored the periphery or the centre area of the arena was evaluated as a measure of anxiety-like behaviour.

Novel Object Recognition Test

Long-term memory was evaluated using the Novel Object Recognition Test, using a grey-coloured, non-reflective arena (44 × 44 × 44 cm). All phases of the test were conducted with a low-intensity white light source. In a first habituation phase, mice were placed into the empty arena for 10 min. The habituation phase was followed by the familiarization one, in which two identical objects (A′ and A″) were presented to each animal for 10 min. Twenty-four hours later, during the testing phase, the same animals were exposed to one familiar object (A″) and a new object (B) for 10 min. A measure of the spontaneous recognition memory was represented by the index of discrimination, calculated as (time exploring the novel object – time exploring the familiar object) / (time exploring both objects) × 100. Mice exploring for less than 7 s were excluded from the analysis due to their inability to perform the task.

Grip-strength test

Mice were lifted by the lower back and tail and lowered towards the grip (Ugo Basile) until they grabbed it with both front paws. The animals were then lowered towards the platform and gently pulled straight back with consistent force until they released their grip. The forelimb grip force, measured in grams, was recorded. The test was repeated five times, and measurements were averaged. After testing, animals were placed back into their home cage.

Paw-clasping test

Mice were suspended by the tail for 30 s and the clasping phenotype was graded according to the following scale: level 0, no clasping; level 1, one hindlimb retracted towards the abdomen; level 2, both hindlimbs retracted towards the abdomen; and level 3, both hindlimbs entirely retracted and touching the abdomen. After testing, animals were placed back into their home cage.

Statistics

Prism 8 (GraphPad software) was used to perform all statistical analyses. Data are presented as means ± standard error of the mean (SEM). Grubbs' test was applied to identify outliers. For each set of data to be compared, we determined whether data were normally distributed or not to select parametric or not parametric statistical tests. The specific statistical test used is indicated in the legend of all results in the figures. Differences were considered statistically if the P-value was less than 0.05. To predetermine sample sizes, we used G-power analysis based on pilot or previous studies. For animal studies, mice were assigned randomly and sex was balanced in the various experimental groups; animals from the same litter were divided in different experimental groups; blinding of the investigator was applied to in vivo procedures and

all data collection. Supplementary Table 2 summarizes all the trials and readouts performed.

Data availability

This study does not include data deposited in public repositories. Data are available on request to the corresponding author.

Results

Setting up a method for SREBP2 delivery to striatal astrocytes *in vivo*

To over-express hSREBP2 in astrocytes *in vivo* in Huntington's disease mice, we used a recombinant serotype of an adeno-associated virus (AAV2/5) that is known to be highly specific for glial cells.[35] We modified the vector backbone to express the tdTomato reporter gene under the control a glial promoter, gfaABC1D,[36] a truncated variant of the human *GFAP* promoter (AAV2/5-gfaABC1D-tdTomato) or fused in-frame with the sequence corresponding to the N-terminal active fragment of human SREBP2 (AAV2/5-gfaABC1D-hSREBP2). We first verified the spread and tropism over time of the AAV2/5-gfaABC1D-tdTomato vector using an *in vivo* method compatible with its application to the Huntington's disease mouse model herein employed (Fig. 1A). Seven-week-old wild-type mice were administered a single unilateral intracranial injection of virus directly into the striatum. Four weeks later, animals were euthanized and subjected to different analyses, as summarized in Fig. 1B. Analysis of coronal sections of the brain by confocal microscopy demonstrated broad distribution of the AAV2/5-gfaABC1D-tdTomato in the infused striatum and in some parts of the cortex, indicating good spread from the injection site. In particular, tdTomato fluorescence was detectable over a span of 2.5 mm and it covered 61.51%±4.85 of the infused hemibrain (Fig. 1C). AAV2/5-gfaABC1D-tdTomato tropism was analysed by studying the co-localization of the tdTomato signal with the signals of neuronal (DARPP32, NeuN) or astrocytic (GFAP, S100B) markers. We found that 80–90% of GFAP- or S100B-positive cells co-localized with tdTomato (Fig. 1D). In contrast, no double-positive cells for tdTomato and neuronal markers were found, demonstrating the specific tropism for glial cells.

An increased number of GFAP-positive astrocytes and of IBA1-positive reactive microglial cells (with amoeboid morphology) was found in the infused striatum of infected mice (Supplementary Fig. 1A–D), suggesting gliosis on AAV infection. Furthermore, about 40% of IBA1-positive cells apparently coexpressed tdTomato and 35% of these cells were reactive microglia with amoeboid morphology (Supplementary Fig. 1E and F). These findings suggest that, at least in this experimental paradigm, reactive microglia may be infected by AAV2/5. It cannot be excluded, however, that IBA1-positive processes envelop tdTomato-positive cells, leading to a false impression of co-localization.

A parallel study conducted by employing a recombinant herpes simplex virus 1 (HSV1) vector as a backbone to deliver the same gfaABC1D-tdTomato construct (Supplementary Fig. 2A) resulted in a widespread expression of the transgene throughout the injected striatum, although exclusively confined in neurons (Supplementary Fig. 2B and C). We therefore proceeded with AAV2/5 to express hSREBP2 in astrocytes in R6/2 mice.

Delivery of AAV2/5-gfaABC1D-hSREBP2 to the Huntington's disease striatum

To establish the efficiency of the *hSrebp2* transgene expression *in vivo*, AAV2/5-gfaABC1D-tdTomato or AAV2/5-gfaABC1D-hSREBP2 were injected into the right striatum of 7-week-old R6/2 mice (herein R6/2-Tom or R6/2-hBP2, respectively), a well-known Huntington's disease animal model characterized by rapidly developing symptoms.[24] Four weeks later, when mice were at the end of the symptomatic stage, cortical and striatal tissues were collected and RNA transcripts and relative amounts of hSREBP2 protein were measured. For this experiment we decided to pool the cortex and striatum because in our preliminary analyses (Fig. 1C) some viral spread was also observed in the cortex.

As shown in Supplementary Fig. 3A, RNA transcripts of *tdTomato* were not detected in the cortico-striatal samples of uninfected wild-type and R6/2 mice, while they were detected and quantified in R6/2-Tom and R6/2-hBP2 samples. Western blotting revealed a tdTomato immunoreactive band in the protein lysates from all R6/2-Tom injected mice but not from the R6/2-hBP2 mice, indicating that *tdTomato* fused downstream to *hSrebp2* was not translated in AAV2/5-gfaABC1D-hSREBP2 infected cells due to an unexpected stop codon at the end of the *hSrebp2* sequence (Supplementary Fig. 3B and C).

As expected, RNA transcripts of *hSrebp2* were detected only in R6/2-hBP2 mice (Fig. 1E). As there are no antibodies available that reliably distinguish human from mouse SREBP2 (mSREBP2), we were not able to calculate the amount of the vector-derived hSREBP2 protein in the infected R6/2-hBP2 mice compared with the endogenous mSREBP2. To overcome this problem, we designed sets of primers to selectively quantify the absolute mRNA levels of *mSrebp2* and *hSrebp2* by RT-qPCR. Notably, we measured a significant reduction of the endogenous *mSrebp2* transcripts in R6/2, R6/2-Tom and R6/2-hBP2 mice compared with wild-type mice (Supplementary Fig. 3D). Importantly, *hSrebp2* mRNA was between 1.7- and 2.1-fold more abundant than the endogenous transcript in R6/2-hBP2 mice (Fig. 1F). As these are whole-tissue measurements, it is expected that mRNA level in the individually transduced cells may be higher. Importantly, western blot analysis with an antibody that recognizes both the endogenous (mouse) and exogenous (human) SREBP2 revealed an increase in total SREBP2 protein level in three of four R6/2-hBP2 mice (Fig. 1G). The over-expression of hSREBP2 and its nuclear translocation was confirmed in additional R6/2-hBP2 mice by immunofluorescence staining for SREBP2. The relative quantification showed a marked increase in nuclear distribution of SREBP2 in the infused striatum (~46.6%) of R6/2-hBP2 mice compared with the contralateral striatum (~11.7%) (Fig. 1H and I). The co-localization of hSREBP2 with astrocytes in the infused striatum was confirmed further by immunofluorescence staining for SREBP2 coupled to the astrocytic markers GFAP and S100B, as shown by the stitched images of the entire brain sections and by high-magnification images (Fig. 1J).

Glial hSREBP2 over-expression enhances cholesterol biosynthesis in Huntington's disease mice

We next sought to test whether the AAV2/5-gfaABC1D-hSREBP2 construct expresses a functional SREBP2 protein capable of increasing transcription of SREBP-controlled genes in the cholesterol biosynthesis pathway.

Gene expression analysis was performed on the pooled striatum and cortex from the injected hemisphere by measuring transcript levels of cholesterol biosynthesis genes (*Hmgcr*, *Mvk*, *Sqs/Fdft1*, *Cyp51*, *Dhcr7*; Fig. 2A) using RT-qPCR. The mRNA levels from all these genes were significantly reduced in R6/2 and R6/2-Tom mice compared with controls (Fig. 2B–F). Importantly, hSREBP2 over-expression in R6/2 mice rescued the transcript levels of *Hmgcr*, *Mvk*, *Fdft1*, and *Cyp51* (Fig. 2B–E) but not of *Dhcr7* (Fig. 2F). The transcript level of *Cyp46a1*, which encodes the enzyme that catalyses the conversion of cholesterol to 24S-OHC, was reduced in

all R6/2 groups compared with controls but was not affected by exogenous hSREBP2 (Fig. 2G).

To explore whether the increased transcription of SREBP2-controlled genes corresponded to an increased activity of the pathway, we measured cholesterol precursors (lanosterol, lathosterol and desmosterol) as surrogate markers of cholesterol biosynthesis. As expected, the steady-state levels of all cholesterol precursors were reduced in the striata of R6/2-Tom mice compared with wt-Tom mice (Fig. 2H–J).[19,20,37,38] Delivery of hSREBP2 in glial cells, although unable to affect lanosterol and lathosterol levels (Fig. 2H–I), led to a significant increase in desmosterol in the striata of R6/2-hBP2 mice compared with R6/2-Tom mice (Fig. 2J), suggesting a preferential stimulation of the Bloch pathway of cholesterol biosynthesis which is more related to astrocytes[39] (Fig. 2A). This was accompanied by an increase in 24S-OHC (Fig. 2K), consistent with the notion that cholesterol synthesis and catabolism are in balance in the Huntington's disease brain.[21]

To assess whether the enhancement of cholesterol biosynthesis genes following striatal injection of AAV2/5-gfaABC1D-hSREBP2 was accompanied by changes in the expression levels of genes involved in cholesterol efflux (Abca1), transport (Apoe), and uptake (Lrp1), we measured their mRNA levels in cortico-striatal tissues. Abca1 mRNA levels were increased in R6/2, R6/2-Tom and R6/2-hBP2 mice with respect to wild-type mice (Supplementary Fig. 4A), while Apoe and Lrp1 mRNA levels were similar in all conditions (Supplementary Fig. 4B and C), indicating that hSREBP2 delivery in glial cells did not affect transcript levels of these genes. Similarly, AAV2/5-gfaABC1D-hSREBP2 did not influence transcript levels of genes involved in astrocytic homeostasis. The Glt1 mRNA level was similarly reduced in R6/2, R6/2-Tom and R6/2-hBP2 mice compared with controls (Supplementary Fig. 4D), while levels of S100b and Kir4.1 (now Kcnl10) were similar in all groups (Supplementary Fig. 4E and F). The mRNA levels of synapse-related genes such as Bdnf, Cplx2, Shank3, Homer and Gap43, which were altered in R6/2 and R6/2-Tom mice, were not influenced by the forced expression of hSREBP2 in glial cells (Supplementary Fig. 4G–K). Transcript levels of genes related to pathways such as energy and mitochondrial metabolism and autophagy were also not affected by the over-expression of hSREBP2 (Supplementary Fig. 5A–I).

Glial hSREBP2 over-expression influences the levels of synaptic proteins in Huntington's disease mice

Since cholesterol secreted from glial cells participates in synapse formation and maintenance and influences the intracellular distribution of proteins involved in the synaptic machinery,[6] we decided to purify synaptosomes from the infused hemibrains of wt-Tom, R6/2-Tom and R6/2-hBP2 mice and perform semiquantitative western blot analysis for pre- and postsynaptic proteins.

We found that R6/2-Tom mice exhibited higher expression levels of the presynaptic protein SYP than wt-Tom mice and that glial hSREBP2 over-expression completely reversed this parameter (Fig. 2L and M). SNAP25 levels were similar in wt-Tom and R6/2-Tom, while a 38% increase was found in R6/2-hBP2 tissues (Fig. 2L and M). VAMP1 levels were similar in all conditions (Fig. 2L and M).

Regarding the postsynaptic site, our densitometric analyses of the immunoreactive bands indicated a weak but significant increase ($P = 0.0138$) in PSD95 level in R6/2-hBP2 mice compared with wt-Tom and R6/2-Tom animals, even though differences between wt-Tom and R6/2-Tom mice were not observed (Fig. 2N and O). Conversely, SHANK3 levels were similar in all the tested mice, including R6/2-hBP2 mice (Fig. 2N and O). Finally, R6/2-Tom mice exhibited reduced NMDAR1 protein levels compared with wt-Tom

mice, and forced expression of hSREBP2 normalized its levels to that of wt-Tom mice (Fig. 2N and O).

We conclude that glial hSREBP2 over-expression influences and partially reverses altered levels of synaptic proteins in synaptosomes of R6/2 mice.

Glial hSREBP2 over-expression restores synaptic communication in Huntington's disease mice

As R6/2 striatal MSNs exhibit altered synaptic transmission,[40,41] we performed electrophysiological studies to evaluate whether synaptic dysfunction was reversed in R6/2-hBP2 mice.

In these studies, biocytin was included in the patch pipette to *post hoc* recover the morphological details of the recorded neurons (Fig. 3A). We first analysed the passive membrane properties of striatal MSNs from brain slices of wt-Tom, R6/2-Tom and R6/2-hBP2 mice. The membrane capacitance (C_m), which is proportional to cell size, was significantly lower in R6/2-Tom and R6/2-hBP2 MSNs compared with wt-Tom MSNs (Fig. 3B). The input resistance (R_{in}), reflecting the number of ion channels expressed by the cell, was significantly higher in both R6/2-Tom and R6/2-hBP2 MSNs (Fig. 3C).

To evaluate the effect of glial cholesterol on excitatory transmission, we recorded sEPSCs at a holding potential of –70 mV (Fig. 3D). The recorded events were AMPA-mediated since they were completely abolished by administration of 10 μM NBQX (Fig. 3D). No significant differences in the average amplitude of sEPSC from MSNs were found between groups (Fig. 3E). In contrast, the average frequency of sEPSCs from MSNs of R6/2-Tom mice was significantly lower compared with MSNs of wt-Tom mice, and glial over-expression of hSREBP2 led to a partial rescue of this defect (Fig. 3F).

To test whether the inhibitory synapses were also influenced by hSREBP2 transduction, we recorded sIPSCs at a holding potential of 0 mV (Fig. 3G). The recorded events were GABA-mediated since they were completely abolished by administration of 10 μM bicuculline (Fig. 3G). The average amplitude of sIPSCs was not affected (Fig. 3H). In contrast, the average frequency of sIPSCs from MSNs of R6/2-Tom mice was significantly higher compared with wt-Tom mice. Notably, glial over-expression of hSREBP2 normalized this defect in MSNs of R6/2-hBP2 mice (Fig. 3I), bringing it closer to that in MSNs of the wt-Tom mice.

By applying the Na$^+$ channel blocker TTX, we also measured action potential-independent postsynaptic events, mEPSCs and mIPSCs. The frequency of these events reflects the probability of stochastic release of synaptic vesicles from the presynaptic terminals and it is also correlated with the number of synapses. We did not find significant differences in the amplitude of these events between groups (Fig. 3J and L). On the contrary, we found that the frequency of mEPSC and mIPSCs was reduced and increased, respectively, in R6/2-Tom MSNs compared with wt-Tom MSNs. Importantly, mEPSC and mIPSC frequency was normalized in R6/2-hBP2 MSNs with similar values to that those wt-Tom MSNs (Fig. 3K and M). As a further control, we measured passive membrane properties and synaptic currents in R6/2-hBP2 MSNs contralateral to the infusion site and found that they were similar to those recorded in R6/2-Tom MSNs (Supplementary Fig. 6A–L).

Glial hSREBP2 over-expression reduces muHTT aggregates in Huntington's disease mice

A hallmark of Huntington's disease is the presence of intracellular aggregates of muHTT.[42] To test whether glial over-expression of hSREBP2 in the Huntington's disease striatum influenced muHTT aggregation, we performed immunofluorescence staining on
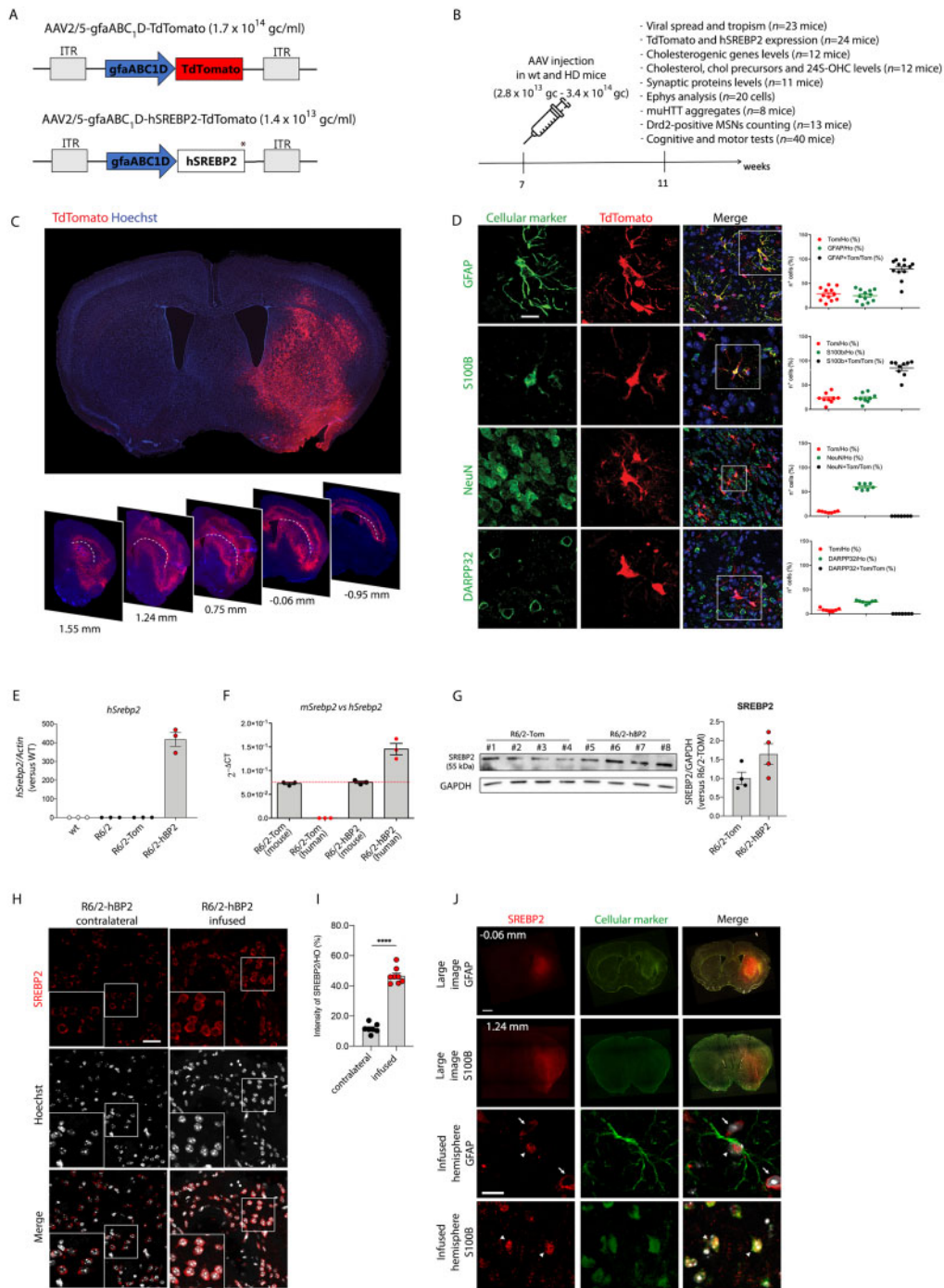
Figure 1 *In vivo* characterization of AAV2/5-gfaABC1D-tdTomato and AAV2/5-gfaABC1D-hSREBP2. (**A** and **B**) Scheme of the AAV vectors (**A**), the experimental paradigm used in the study, and readouts performed (**B**). Mice at 7 weeks of age were infected in the right striatum with AAV2/5 vectors and euthanized 4 weeks later. An asterisk indicates an unexpected stop codon that was accidentally inserted immediately after the *hSrebp2* sequence during the cloning preventing *tdTomato* translation. (**C**) Representative immunofluorescence large images showing diffusion of tdTomato (red) in coronal brain slices of wild-type (wt) mice infected with AAV2/5-gfaABC1D-tdTomato. (**D**) Representative immunofluorescence images showing tdTomato-labelled cells (red), GFAP and S100b labelled astrocytes (green) and NeuN and DARPP32 labelled neurons (green) in coronal brain slices of mice infected with AAV2/5-gfaABC1D-TdTomato and relative quantification of the number of cells double positive for tdTomato and for the specific cellular marker, normalized on the number of the nuclei in the field of view (expressed as per cent). (**E** and **F**) Messenger RNA levels of human *SREBP2* (*hSrebp2*) (**E**) and mouse *Srebp2* (*mSrebp2*) (**F**) in the hemibrains from wild-type (wt), R6/2, R6/2-Tom and R6/2-hBP2 mice normalized on wild-type (wt) mice (n = 3 mice/group). (**G**) Level of SREBP2 protein and relative densitometric quantification in protein lysates from the infused hemibrains of R6/2-Tom or R6/2-hBP2 (n = 4 mice/group). GAPDH was used as loading control and for normalization. (**H** and **I**) Representative immunofluorescence image of SREBP2-labelled cells (**H**) and relative quantification (**I**) in the infused and contralateral striatum of R6/2-hBP2 mice (n = 4 mice). (**I**) Graph represents the intensity of SREBP2 normalized on nuclei (%). (**J**) Representative immunofluorescence large image and high-magnification image of the infused striatum with SREBP2 (red) and GFAP- or S100B-labelled cells (green) in coronal brain slices of R6/2-hBP2 mice. Nuclear (triangles) and perinuclear (arrows) localization of SREBP2 is indicated. Hoechst was used to counterstain nuclei (blue in **C** and **D**, grey in **H** and **J**). Scale bars = 1000 μm (**C**), 5 μm (**D**), 20 μm (**H**), 2000 μm (**J**, large image) and 10 μm (**J**, crop). Data (**E–G** and **I**) are shown as scatter plot graphs with means ± SEM. Each dot corresponds to the value obtained from one image (**D** and **I**) or from each animal (**E–G**). Statistics: unpaired Student's *t*-test (****P < 0.0001).
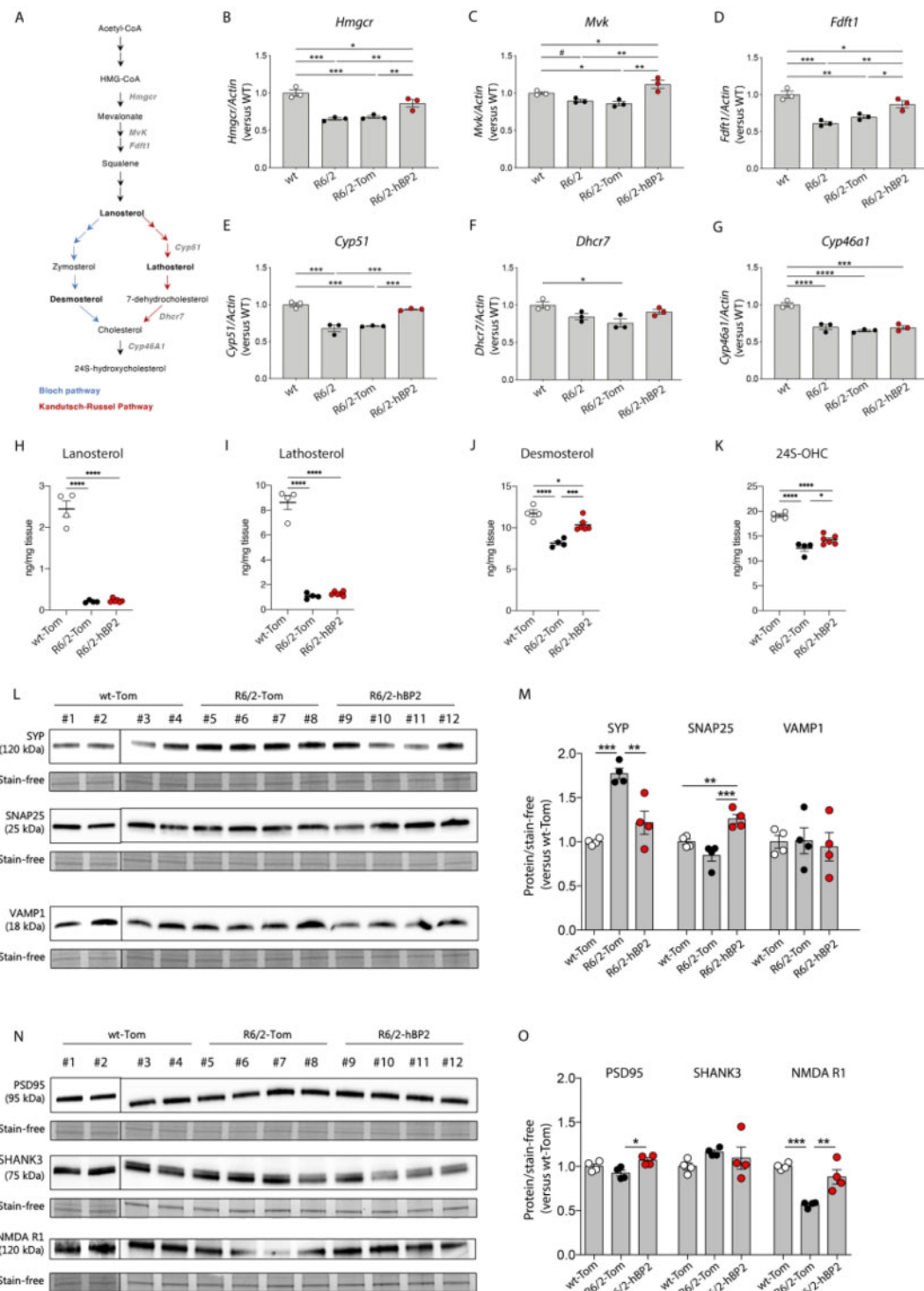
Figure 2 Messenger RNA transcript levels of cholesterol biosynthesis genes and levels of synaptic proteins following glial hSREBP2 over-expression. (**A**) Genes encoding enzymes of cholesterol biosynthesis whose expression was analysed by RT-qPCR (grey). Products of the Bloch and Kandutsch–Russell pathways are in blue and red, respectively. (**B–G**) Messenger RNA levels of *Hmgcr* (**B**), *Mvk* (**C**), *Sqs/Fdft1* (**D**), *Cyp51* (**E**), *Dhcr7* (**F**) and *Cyp46a1* (**G**) in the hemibrain from wild-type (wt), R6/2, R6/2-Tom mice and R6/2-hBP2 mice (*n* = 3 mice/group). (**H–K**) Lanosterol (**H**), lathosterol (**I**), desmosterol (**J**) and 24-OHC (**K**) levels in the infused striata of wt-Tom, R6/2-Tom and R6/2-hBP2 mice (*n* = 4–6 mice/group). (**L** and **M**) Protein levels (**L**) and relative densitometric quantification (**M**) of SYP, SNAP25 and VAMP1 in synaptosomes purified from the infused hemibrains from wt-Tom mice, R6/2-Tom mice and R6/2-hBP2 mice (*n* = 4 mice/group). (**N** and **O**) Protein levels (**N**) and relative densitometry quantification (**O**) of PSD95, SHANK3 and NMDAR1 in synaptosomes purified from the infused hemibrains from wt-Tom mice, R6/2-Tom mice and R6/2-hBP2 mice (*n* = 4 mice/group). Stain-free imaging (in **L** and **N**) was used as a loading control and for normalization. Data (**B–K**, **M** and **O**) are shown as scatter plot graphs with means ± SEM. Each dot corresponds to the value obtained from each animal. See Supplementary Figs 8 and 9 for full-length pictures of the blots shown in **L** and **N**. Statistics: one-way ANOVA with Newman–Keuls *post hoc* test (*$P < 0.05$; **$P < 0.01$; ***$P < 0.001$; ****$P < 0.0001$) or unpaired Student's *t*-test ([#]$P < 0.05$).
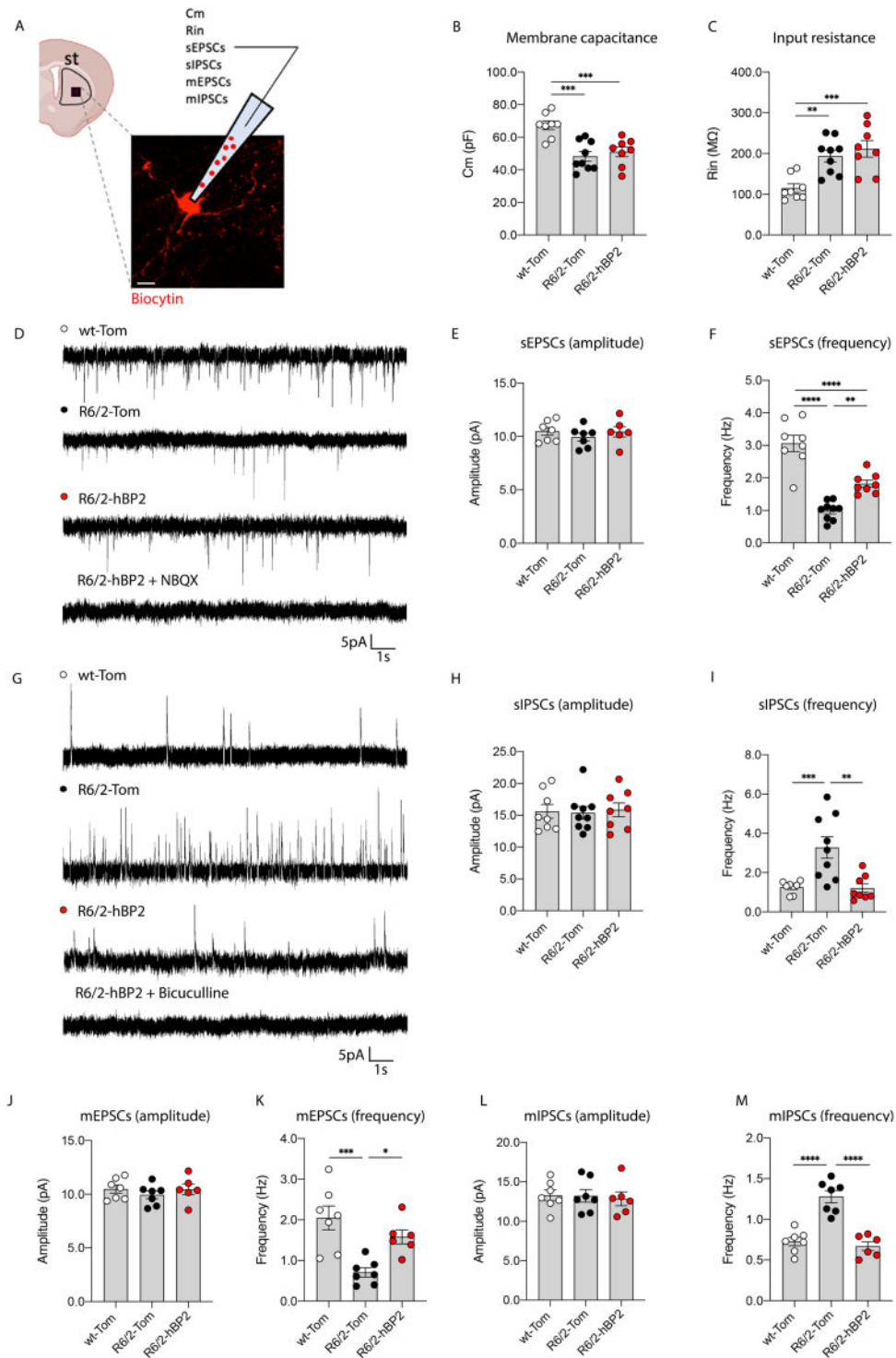
Figure 3 Electrophysiological analysis in MSNs of R6/2 mice following glial hSREBP2 over-expression. (**A**) Schematic representation of the electrophysiological parameters analysed in striatal MSNs of mice following 4 weeks of AAV infusion and representative image of the recorded cells with biocytin. Scale bar = 5 μm. (**B** and **C**) Membrane capacitance (C_m, **B**) and input resistance (R_{in}, **C**) recorded from MSNs of wt-Tom, R6/2-Tom and R6/2-hBP2 mice. (**D–F**) Representative traces of sEPSCs recorded from striatal MSNs of wt-Tom, R6/2-Tom and R6/2-hBP2 mice at a holding potential of −70 mV (**D**). Average amplitude (**E**) and average frequency (**F**) of sEPSCs recorded from MSNs of wt-Tom, R6/2-Tom and R6/2-hBP2 mice. (**G–I**) Representative traces of sIPSCs recorded from MSNs of wt-Tom, R6/2-Tom and R6/2-hBP2 mice at a holding potential of 0 mV (**G**). Average amplitude (**H**) and average frequency (**I**) of sIPSCs recorded from MSNs of wt-Tom, R6/2-Tom and R6/2-hBP2 mice. (**J–M**) Average amplitude and frequency of mEPSCs (**J** and **K**) and of mIPSCs (**L** and **M**) recorded from wt-Tom, R6/2-Tom and R6/2-hBP2 MSNs, in presence of the Na$^+$ channel blocker TTX (1 μM). Data (**B**, **C**, **E**, **F** and **H–M**) are shown as scatter plot graphs with means ± SEM. Each dot corresponds to the value obtained from each cell ($n = 3$–5 mice/group). Statistics: one-way ANOVA with Newman–Keuls *post hoc* test (*$P < 0.05$; **$P < 0.01$; ***$P < 0.001$; ****$P < 0.0001$).

coronal sections of brains from R6/2-Tom and R6/2-hBP2 mice by using the EM48 antibody, which is specific for the expanded polyQ tract prone to aggregate (Fig. 4A). As expected, tdTomato did not influence the number and the size of muHTT aggregates. Of note, the number and the size of EM48-positive aggregates were reduced in the infused striata of R6/2-hBP2 mice compared with the contralateral ones (Fig. 4B and C). Furthermore, double immunofluorescence staining with EM48 antibody in combination with antibodies against NeuN (a neuronal marker), DARPP32 (an MSN marker), S100B, and GFAP (astrocyte markers) was performed to count the number of nuclear muHTT aggregates in the striatum of R6/2-hBP2 mice in different cell types. In all the cell types analysed, the number of nuclear aggregates was significantly reduced in the infused compared with the contralateral striatum of R6/2-hBP2 mice (Fig. 4D and E).

To further confirm the reduction of muHTT aggregates, we performed semiquantitative western blot analysis on synaptosomes isolated from the infused hemibrains of wt-Tom, R6/2-Tom and R6/2-hBP2 mice, to detect SDS-insoluble muHTT. As shown in Supplementary Fig. 7A and B, muHTT aggregates are significantly decreased in synaptosomes of R6/2-hBP2 mice compared to R6/2-Tom mice.

To explore whether SREBP2 co-localized with aggregated muHTT *in vivo* following AAV2/5-hSREBP2, immunofluorescence staining for SREBP2 together with EM48 antibody, which recognizes muHTT aggregates, was performed in brain slices of R6/2-hBP2 mice. SREBP2 did not co-localize with muHTT aggregates in R6/2-hBP2 mice (Supplementary Fig. 7C) but co-localized with total muHTT (as detected by MAB2166 antibody) (Supplementary Fig. 7D), suggesting that *in vivo*, in the R6/2 mouse brain, the active SREBP2 interacts with muHTT but it is not sequestered in aggregates.

Glial hSREBP2 over-expression increases Drd2-expressing MSN number in Huntington's disease mice

Neuronal dysfunction of striatal neurons precedes their degeneration, and the dopamine receptor D2 (DRD2) MSNs of the indirect pathway are the first affected in Huntington's disease models and patients.[43–46] Although R6/2 mice (similar to other Huntington's disease mouse models) do not show overt signs of neuronal loss,[24] the downregulation of *Drd2* transcript in striatal MSNs is an established early mark of disease progression that has been proposed as a sensitive measure of the effects of therapeutics.[47] In particular, Crook and Housman developed a Drd2 dysregulation assay by crossing Drd2-eGFP mice with different Huntington's disease mice to obtain animals with DRD2-MSNs labelled with eGFP, and then used FACS sorting as a quantitative and reproducible readout of the efficacy of their therapeutics.[47]

Here we adopted a similar strategy by crossing R6/2 mice with animals having DRD2-MSNs expressing eGFP (herein Drd2-wt and Drd2-R6/2 mice) and by using the CLARITY, a tissue clearing technology that allows to obtain an accurate measurement of the total number of MSNs expressing DRD2 in a large volume of the vector-injected striatum ($\sim108 \pm 5\,\mu m^3$), without dissociation.

To accomplish this goal, we injected AAV2/5-gfaABC1D-tdTomato or AAV2/5-gfaABC1D-hSREBP2 into the right striata of 7-week-old Drd2-wt and Drd2-R6/2 mice (herein Drd2-wt-Tom, Drd2-R6/2-Tom and Drd2-R6/2-hBP2). Animals were euthanized 4 weeks later. From each animal, two brain coronal slices that were 1 mm thick (including the striatum) were prepared from the infused and contralateral hemispheres and the area corresponding to the striatum was isolated and clarified using the CLARITY technology (Fig. 4F). The images acquired with two-photon microscopy

in the clarified striata of Drd2-wt-Tom mice confirmed distinct signals of tdTomato and eGFP, which labelled infected glial cells and DRD2-MSNs, respectively (Fig. 4G). The subsequent quantification of the eGFP signal in the different experimental groups revealed a reduced number of DRD2-MSNs in the infused striata of Drd2-R6/2-Tom mice and in the contralateral striata of Drd2-R6/2-hBP2 compared with Drd2-wt-Tom mice (Fig. 4H and I). Of note, the number of DRD2-MSNs measured in the infused striata of Drd2-R6/2-hBP2 was similar to that quantified in Drd2-wt-Tom mice (Fig. 4H and I), indicating that over-expression of hSREBP2 in astrocytes allows these neurons to regain DRD2 expression and, supposedly, functionality.

Glial hSREBP2 over-expression ameliorates motor defects and restores cognitive decline in mice

To assess whether the described amelioration of synaptic activity and disease phenotypes following over-expression of hSREBP2 in astrocytes was correlated with a beneficial effect on behavioural abnormalities, we subjected wt-Tom, R6/2-Tom and R6/2-hBP2 mice to motor and cognitive tasks.

As expected, 11-week-old R6/2-Tom mice exhibited a severe hypokinetic phenotype as demonstrated by reduced global activity, total distance travelled and number of rearings in the activity cage test (Fig. 5A–C). Glial over-expression of hSREBP2 led to a slight but significant rescue of these parameters (Fig. 5A–C). We also evaluated the time that mice spent exploring the peripheral or central area of the arena during the activity cage test as a measure of anxiety-like behaviour (Fig. 5D). R6/2-Tom mice showed anxiety-related behaviour as they spent more time in the periphery compared with wt-Tom mice. Of note, R6/2-hBP2 mice behaved similarly to wt-Tom mice (Fig. 5E). When we measured the neuromuscular function of mice with the grip-strength test, we observed reduced muscle strength in R6/2-Tom mice compared with wt-Tom mice and, again, glial over-expression of hSREBP2 had a beneficial effect on this feature (Fig. 5F). Furthermore, we performed the paw-clasping test to study the clasping behaviour of mice as an index of neuronal dysfunction. As expected, R6/2-Tom mice had a worse performance compared with wt-Tom, but in this case the treatment was not able to significantly rescue this behaviour (Fig. 5G). Finally, to analyse the effect of treatment on recognition memory, a subcategory of declarative memory impaired in Huntington's disease models, we performed the Novel Object Recognition Test: at 11 weeks of age, R6/2-Tom mice were not able to discriminate between the novel object and the familiar one, in contrast to the wt-Tom mice. Of note, glial over-expression of hSREBP2 completely prevented cognitive decline and R6/2-hBP2 mice behaved as the wt-Tom (Fig. 5H).

Discussion

In this work, we highlight the biological value of forcing cholesterol biosynthesis *in vivo* in the R6/2 Huntington's disease mouse model via a gene therapy approach that delivers the N-terminal active fragment of the master transcription factor SREBP2 specifically to astrocytes. In the brain, the physiological cross-talk between astrocytes and neurons provides the latter with the cholesterol produced by the former, which is then used by neurons to support their function. This cross-talk is severely damaged in Huntington's disease astrocytes due to reduced nuclear levels of the active SREBP2. Of note, the over-expression of the active SREBP2 in Huntington's disease astrocytes fully re-establishes neuronal function and morphology in cocultured Huntington's disease neurons.[22] Here, we now provide *in vivo* evidence that this altered communication between astrocytes and neurons is a key
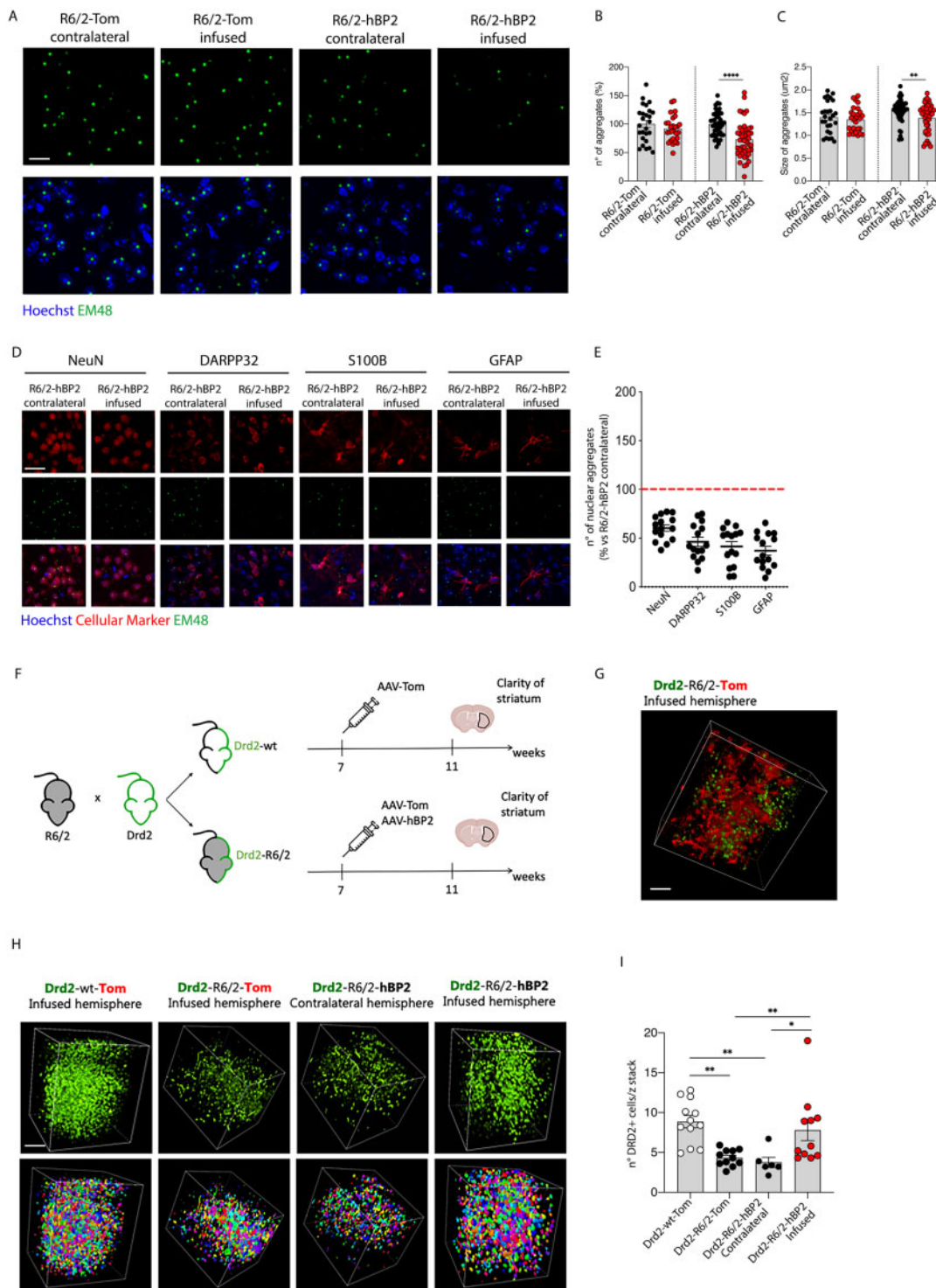
Figure 4 Mutant HTT aggregation and number of Drd2 neurons in R6/2 mice following glial hSREBP2 over-expression. (A–C) Representative immunofluorescence images of muHTT aggregates positive for EM48 antibody (green) (A) and relative quantification of number (B) and size (C) in infused and contralateral striata of R6/2-Tom mice or R6/2-hBP2 mice ($n = 3$–5/group). The number of muHTT aggregates (B) in the infused hemisphere was normalized on the contralateral one. (D and E) Representative immunofluorescence images showing muHTT aggregates (EM48 antibody, green) in NeuN and DARPP32 labelled neurons (red) or in S100B and GFAP labelled astrocytes (red) (D) in infused and contralateral striata of R6/2-hBP2 mice ($n = 3$/group), and relative quantification of the number of muHTT aggregates in the infused hemisphere normalized on the contralateral one (E). (F) Experimental paradigm used in the CLARITY experiment. R6/2 mice were crossed with mice having Drd2-expressing MSNs tagged with GFP to obtain a line with GFP-MSNs neurons from the indirect pathway ($n = 4$–5 mice/group). (G) Representative two-photon image of the endogenous signals of GFP (green) and TdTomato (red) of 1-mm thick brain coronal slices from Drd2-wt-Tom (infused hemisphere). (H and I) Representative two-photon images (H, *top*) of the endogenous signal of GFP (green) of 1-mm thick brain coronal slices from Drd2-wt-Tom (infused hemisphere), Drd2-R6/2-Tom (infused hemisphere), and Drd2-R6/2-hBP2 (contralateral and infused hemisphere) with relative 3D reconstruction (H, *bottom*) and quantification of the number of neurons normalized on the z-stack acquired (I). Data (B, C, E and I) are shown as scatter plot graphs with means ± SEM. Each dot corresponds to an image from 3–5 mice/group. Hoechst (blue) (A and D) was used to counterstain nuclei. Scale bars = 10 μm (A), 25 μm (D), 100 μm (G) and 200 μm (H). Statistics: one-way ANOVA with Newman–Keuls *post hoc* test (*P < 0.05; **P < 0.01; ****P < 0.0001).
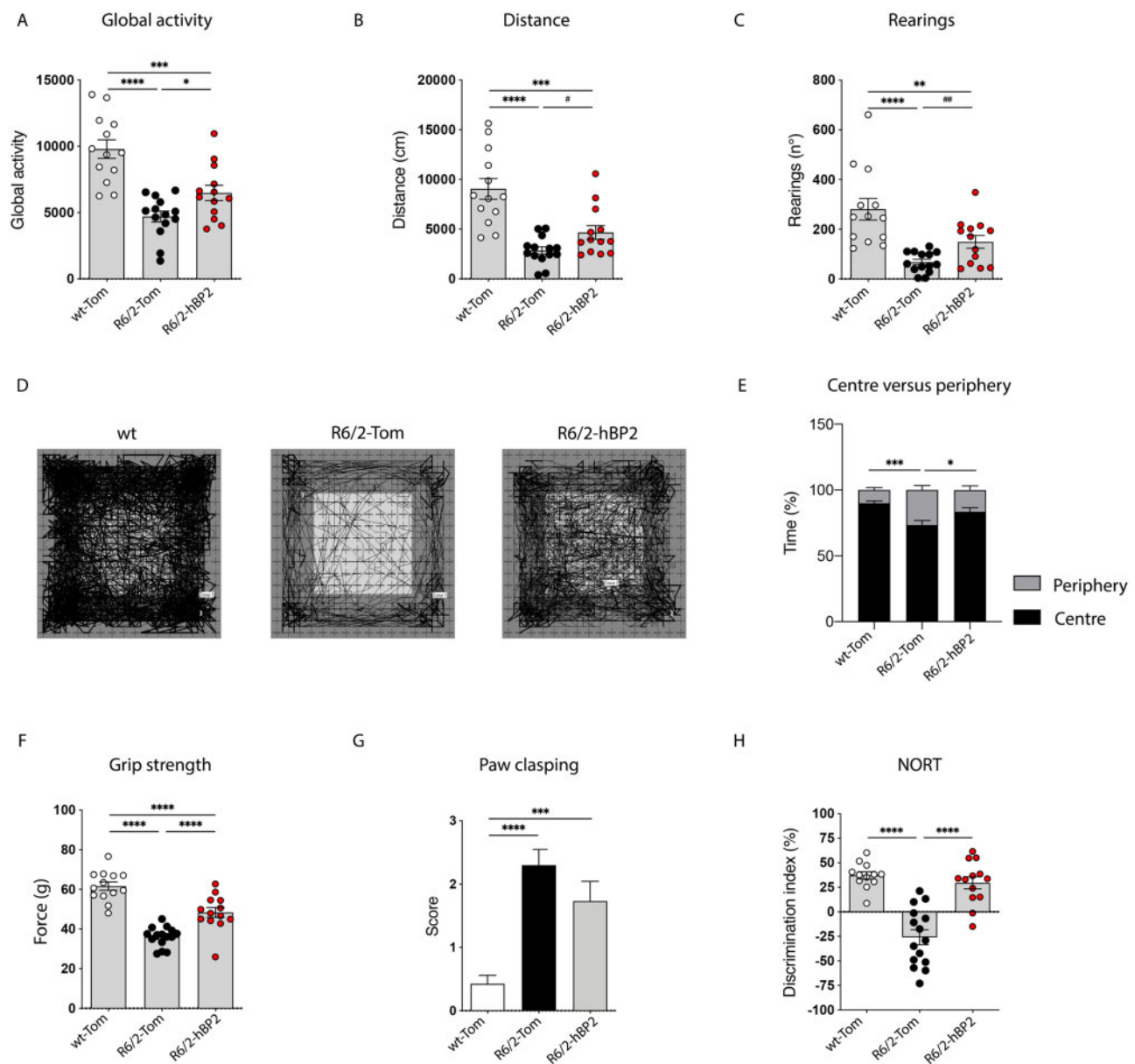
Figure 5 Cognitive and motor abilities of R6/2 mice following glial hSREBP2 over-expression. (**A–E**) Global activity (**A**), distance travelled (**B**), and number of rearings (**C**) in an open-field test in wt-Tom ($n = 13$), R6/2-Tom ($n = 14$) and R6/2-hBP2 ($n = 13$). Representative track plots (**D**) from the open-field test from wt-Tom ($n = 13$), R6/2-Tom ($n = 14$) and R6/2-hBP2 ($n = 13$) and relative quantification (**E**) of the time spent (%) in the centre and in the periphery of the arena. (**F**) Grip strength (grams) in wt-Tom ($n = 13$), R6/2-Tom ($n = 15$), and R6/2-hBP2 ($n = 13$). (**G**) Paw clasping in wt-Tom ($n = 13$), R6/2-Tom ($n = 15$), and R6/2-hBP2 ($n = 13$). (**H**) Discrimination index (DI %) in the Novel Object Recognition Test (NORT) of wt-Tom ($n = 12$), R6/2-Tom ($n = 15$) and R6/2-hBP2 ($n = 13$). DI above zero indicates a preference for the novel object; DI below zero indicates a preference for the familiar object. Data (**A–C** and **F–H**) are shown as scatter plot graphs with means ± SEM and each dot corresponds to the value obtained from each animal. Data (**E** and **G**) are shown as histograms with means ± SEM. Statistics: one-way ANOVA with Newman–Keuls *post hoc* test (*$P < 0.05$; **$P < 0.01$; ***$P < 0.001$; ****$P < 0.0001$) or unpaired Student's *t*-test (#$P < 0.05$; ##$P < 0.01$).

pathological feature of astrocytes, which can be targeted at a cellular level and their pathology reversed, leading to substantial amelioration of Huntington's disease phenotypes in the living animals. Accordingly, we show that hSREBP2 delivery to astrocytes *in vivo*, by enhancing the cholesterol biosynthesis pathway, can revert molecular, biochemical, electrophysiological and behavioural abnormalities associated with neuronal dysfunction typically observed in the R6/2 mouse model.

We show that unilateral striatal AAV delivery of hSREBP2 in glial cells is sufficient to completely rescue cognitive decline in R6/2 mice. Similar data were obtained on cholesterol delivery to

the brain of this mouse model via brain-permeable polymeric nanoparticles or mini-pumps.[37,38] The fact that genetic deletion of SCAP or SREBP2 in astrocytes of adult mice results in cognitive defects[48,49] confirms the role of astrocytes in memory and cognition *in vivo*, and that altered cross-talk between astrocytes and neurons at synaptic contacts may contribute to cognitive disturbances.[50] Moreover, cholesterol synthesis is downregulated in ageing astrocytes,[51,52] suggesting that lack of cholesterol production in these cells may contribute to the synaptic and cognitive defects observed in ageing. Here, we provide further evidence that cholesterol produced from astrocytes *in vivo* is also a critical

player in recognition memory in the Huntington's disease context.

Unilateral striatal AAV delivery of hSREBP2, by diffusing in almost all the striatum and in some part of the cortex, also ameliorated motor defects in R6/2 mice, suggesting that this approach is able to produce the optimal content of newly synthetized cholesterol needed to partially restore motor-dependent circuits. These results are in agreement with our recent work demonstrating that three escalating doses of cholesterol unilaterally infused into the striata of R6/2 mice through osmotic mini-pumps prevented cognitive defects, while only the highest dose attenuated motor phenotypes.[38] Surprisingly, the functional recovery in one hemisphere was sufficient, in both strategies, to compensate for global deficits and to perform some tasks correctly. More work will be needed to explore the mechanism(s) underlying these intriguing observations.

Mechanistically, our findings indicate that hSREBP2 over-expression in glial cells carries out its beneficial effect by acting on different aspects of the disease. The synaptic effect of AAV delivery of hSREBP2 is certainly the relevant one, and it is supported by the evidence of normalization in the level of synaptic proteins and of both inhibitory and excitatory synaptic communication of MSNs. Newly synthetized cholesterol from astrocytes may facilitate synaptic vesicle fusion and exocytosis[53] or bind to proteins involved in synaptic transmission.[8,54] Of note, the normalization of the frequency of miniature events, a parameter that measures spontaneous vesicular fusion events and is related to the number of synapses, highlights a key presynaptic role of glial cholesterol to restore optimal neurotransmitter release.

Our current data also indicate that the mechanisms by which stimulation of cholesterol biosynthesis counteracts synaptic dysfunction in Huntington's disease mice do not involve major transcriptional changes since mRNA levels of key synaptic genes, which are known to be altered in Huntington's disease, are unaffected by hSREBP2 delivery. Nor are the mRNA levels of a subset of genes involved in glial or energy metabolism influenced by exogenous hSREBP2.

At the neuropathological level, striatal delivery of hSREBP2 in R6/2 mice reduced the number and size of muHTT aggregates. In particular, nuclear muHTT aggregates were decreased not only in astrocytes but also in neurons, suggesting that muHTT clearance may also occur by a non-cell autonomous mechanism. Although further studies are needed to explore the underlying mechanism, a direct role of SREBP2 to counteract aggregates is unlikely, since SREBP2 does not co-localize with EM48-positive aggregated muHTT. Instead, we hypothesize that the enhancement of cholesterol biosynthesis (i.e. increased desmosterol level or newly synthetized cholesterol itself) following AAV2/5-gfaABC1D-hSREBP2 may induce clearance pathways, as we recently showed in the striata of R6/2 mice following striatal infusion of cholesterol through osmotic mini-pumps.[38] In keeping with this hypothesis, cholesterol precursors are known to reduce aggregation of misfolded proteins in cataract and neurodegeneration models.[55–58]

Importantly, hSREBP2 over-expression in glial cells rescues specific neurochemical features in MSNs. In fact, reduced striatal DRD2 was consistently demonstrated in patients[59–63] and murine models[37,45,64,65] and its dysregulation is a sensitive measure of Huntington's disease pathology.[47] Of note, a loss of dopamine receptors has also been correlated with early cognitive decline.[66] Our CLARITY approach applied to the striatum allowed for the first time an accurate measurement and quantification of striatal MSNs *in situ* and confirmed the decrease in the level of DRD2 in MSNs.[47] Importantly, we show that Huntington's disease neurons, which receive more cholesterol from hSREBP2 over-expressing astrocytes, increase DRD2 expression and are quantifiable through two-photon imaging. These findings also suggest that within the

striatum, the astrocyte-neuron signalling may be synapse- and cell-specific by acting at least on the DRD2-MSNs, as recently proposed.[67] The observed rescue in DRD2-MSNs, and in other synaptic features, may be favoured by a closer contact between neurons and astrocytes, which is reduced in R6/2 astrocytes.[68]

In a similar gene therapy approach, the gene encoding for CYP46A1, the enzyme that converts cholesterol into the neuronal cholesterol catabolite 24S-OHC, was delivered into striatal neurons of Huntington's disease mice by use of an AAVrh10 vector.[58,69] The treatment decreased the number and size of muHTT aggregates and improved motor deficits in R6/2 mice[69] and provided long-lasting improvement in zQ175 Huntington's disease mice.[58] In both studies, levels of cholesterol precursors were restored or increased in the disease striatum following AAV delivery of CYP46A1. In our study, we show increased levels of 24S-OHC following AAV delivery of hSREBP2 in glial cells, although *Cyp46A1* mRNA remained unchanged, supporting the close balance between cholesterol synthesis and catabolism in the diseased brain.

In conclusion, our findings confirm the role of astrocytes as important regulatory cell types in brain function and behaviour[50,70] and in neurodegenerative disorders, including Huntington's disease.[71–72] By targeting astrocytic cholesterol signalling in the striatum we were able to rescue biochemical, neuropathological, functional, and behavioural features in R6/2 mice. These findings help to increase our understanding of the Huntington's disease pathophysiology and may provide the foundation for new therapeutic strategies.

Acknowledgements

Funding

Competing interests

The authors report no competing interests.

Supplementary material

Supplementary material is available at *Brain* online.

References

1. Dietschy JM, Turley SD. Cholesterol metabolism in the central nervous system during early development and in the mature animal. *J Lipid Res*. 2004;45(8):1375–1397.

2. Björkhem I, Meaney S, Fogelman AM. Brain cholesterol: Long secret life behind a barrier. *Arterioscler Thromb Vasc Biol*. 2004; 24(5):806–815.

3. Mauch DH, Nägler K, Schumacher S, et al. CNS synaptogenesis promoted by glia-derived cholesterol. *Science*. 2001;294(5545): 1354–1357.

4. Göritz C, Mauch DH, Nägler K, Pfrieger FW. Role of glia-derived cholesterol in synaptogenesis: New revelations in the synapse-glia affair. *J Physiol Paris*. 2002;96(3-4):257–263.

5. Goritz C, Mauch DH, Pfrieger FW. Multiple mechanisms mediate cholesterol-induced synaptogenesis in a CNS neuron. *Mol Cell Neurosci*. 2005;29(2):190–201.

6. Pfrieger FW. Role of cholesterol in synapse formation and function. *Biochim Biophys Acta*. 2003;1610(2):271–280.

7. Pfrieger FW. Cholesterol homeostasis and function in neurons of the central nervous system. *Cell Mol Life Sci*. 2003;60(6): 1158–1171.

8. Pfrieger FW. Outsourcing in the brain: Do neurons depend on cholesterol delivery by astrocytes? *BioEssays*. 2003;25(1):72–78.

9. Jurevics H, Morell P. Cholesterol for synthesis of myelin is made locally, not imported into brain. *J Neurochem*. 1995;64(2):895–901.

10. Nunes VS, Cazita PM, Catanozi S, Nakandakare ER, Quintão ECR. Decreased content, rate of synthesis and export of cholesterol in the brain of apoE knockout mice. *J Bioenerg Biomembr*. 2018;50(4):283–287.

11. Jeon T, Il, Osborne TF. SREBPs: Metabolic integrators in physiology and metabolism. *Trends Endocrinol Metab*. 2012;23(2):65–72.

12. Yang T, Espenshade PJ, Wright ME, et al. Crucial step in cholesterol homeostasis: Sterols promote binding of SCAP to INSIG-1, a membrane protein that facilitates retention of SREBPs in ER. *Cell*. 2002;110(4):489–500.

13. Valenza M, Cattaneo E. Emerging roles for cholesterol in Huntington's disease. *Trends Neurosci*. 2011;34(9):474–486.

14. Martín MG, Pfrieger F, Dotti CG. Cholesterol in brain disease: Sometimes determinant and frequently implicated. *EMBO Rep*. 2014;15(10):1036–1052.

15. Vonsattel JP, DiFiglia M. Huntington disease. *J Neuropathol Exp Neurol*. 1998;57:369–384.

16. Rüb U, Seidel K, Heinsen H, et al. Huntington's disease (HD): the neuropathology of a multisystem neurodegenerative disorder of the human brain. *Brain Pathol*. 2016;26(6):726–740.

17. Valenza M, Rigamonti D, Goffredo D, et al. Dysfunction of the cholesterol biosynthetic pathway in Huntington's disease. *J Neurosci*. 2005;25(43):9932–9939.

18. Valenza M, Leoni V, Tarditi A, et al. Progressive dysfunction of the cholesterol biosynthesis pathway in the R6/2 mouse model of Huntington's disease. *Neurobiol Dis*. 2007;28(1):133–142.

19. Valenza M, Carroll JB, Leoni V, et al. Cholesterol biosynthesis pathway is disturbed in YAC128 mice and is modulated by huntingtin mutation. *Hum Mol Genet*. 2007;16(18):2187–2198.

20. Valenza M, Leoni V, Karasinska JM, et al. Cholesterol defect is marked across multiple rodent models of Huntington's disease and is manifest in astrocytes. *J Neurosci*. 2010;30(32): 10844–10850.

21. Shankaran M, Di Paolo E, Leoni V, et al. Early and brain region-specific decrease of de novo cholesterol biosynthesis in Huntington's disease: A cross-validation study in Q175 knock-in mice. *Neurobiol Dis*. 2017;98:66–76.

22. Valenza M, Marullo M, Di Paolo E, et al. Disruption of astrocyte-neuron cholesterol cross talk affects neuronal function in Huntington's disease. *Cell Death Differ*. 2015;22(4):690–702.

23. Di Pardo A, Monyror J, Morales LC, et al. Mutant huntingtin interacts with the sterol regulatory element-binding proteins and impairs their nuclear import. *Hum Mol Genet*. 2020;29(3):418–431.

24. Mangiarini L, Sathasivam K, Seller M, et al. Exon 1 of the HD gene with an expanded CAG repeat is sufficient to cause a progressive neurological phenotype in transgenic mice. *Cell*. 1996; 87(3):493–506.

25. Gong S, Zheng C, Doughty ML, et al. A gene expression atlas of the central nervous system based on bacterial artificial chromosomes. *Nature*. 2003;425(6961):917–925.

26. Zoumi A, Datta S, Liaw L-HL, et al. Spatial distribution and function of sterol regulatory element-binding protein 1a and 2 homo- and heterodimers by *in vivo* two-photon imaging and spectroscopy fluorescence resonance energy transfer. *Mol Cell Biol*. 2005;25(8):2946–2956.

27. Arsic N, Zentilin L, Zacchigna S, et al. Induction of functional neovascularization by combined VEGF and angiopoietin-1 gene transfer using AAV vectors. *Mol Ther*. 2003;7(4):450–459.

28. Ayuso E, Mingozzi F, Montane J, et al. High AAV vector purity results in serotype- and tissue-independent enhancement of transduction efficiency. *Gene Ther*. 2010;17(4):503–510.

29. Zentilin L, Marcello A, Giacca M. Involvement of cellular double-stranded DNA break binding proteins in processing of the recombinant adeno-associated virus genome. *J Virol*. 2001; 75(24):12279–12287.

30. Miyagawa Y, Verlengia G, Reinhart B, et al. Deletion of the virion host shut-off gene enhances neuronal-selective transgene expression from an HSV vector lacking functional IE genes. *Mol Ther Meth Clin Dev*. 2017;6:79–90.

31. Paolone G, Falcicchia C, Verlengia G, et al. Personalized needles for microinjections in the rodent brain. *J Vis Exp*. 2018;(131):55751.

32. Paolone G, Watson and C. The Rat Brain in Stereotaxic Coordinates. Academic Press, San Diego.

33. Lloyd MH, Wolfensohn SE. Practical use of distress scoring systems in the application of humane endpoints. In: *International Conference on the Use of Humane Endpoints in Animal Experiments for Biomedical Research*. 1998;36:22–25.

34. Civra A, Leoni V, Caccia C, et al. Antiviral oxysterols are present in human milk at diverse stages of lactation. *J Steroid Biochem Mol Biol*. 2019;193:105424.

35. Tong X, Ao Y, Faas GC, et al. Astrocyte Kir4.1 ion channel deficits contribute to neuronal dysfunction in Huntington's disease model mice. *Nat Neurosci*. 2014;17(5):694–703.

36. Lee Y, Messing A, Su M, Brenner M. GFAP promoter elements required for region-specific and astrocyte-specific expression. *Glia*. 2008;56(5):481–493.

37. Valenza M, Chen JY, Di Paolo E, et al. Cholesterol-loaded nanoparticles ameliorate synaptic and cognitive function in Huntington's disease mice. *EMBO Mol Med*. 2015;7(12):1547–1564.

38. Birolini G, Valenza M, Di Paolo E, et al. Striatal infusion of cholesterol promotes dose-dependent behavioral benefits and exerts disease-modifying effects in Huntington's disease mice. *EMBO Mol Med*. 2020;12:e12519.

39. Pfrieger FW, Ungerer N. Cholesterol metabolism in neurons and astrocytes. *Prog Lipid Res*. 2011;50(4):357–371.

40. Cepeda C, Hurst RS, Calvert CR, et al. Transient and progressive electrophysiological alterations in the corticostriatal pathway in a mouse model of Huntington's disease. *J Neurosci*. 2003;23(3): 961–969.

41. Cepeda C, Starling AJ, Wu N, et al. Increased GABAergic function in mouse models of Huntington's disease: Reversal by BDNF. *J Neurosci Res*. 2004;78(6):855–867.

42. DiFiglia M, Sapp E, Chase KO, et al. Aggregation of huntingtin in neuronal intranuclear inclusions and dystrophic neurites in brain. *Science*. 1997;277(5334):1990–1993.

43. Reiner A, Albin RL, Anderson KD, et al. Differential loss of striatal projection neurons in Huntington disease. *Proc Natl Acad Sci U S A*. 1988;85(15):5733–5737.

44. Albin RL, Young AB, Penney JB. The functional anatomy of basal ganglia disorders. *Trends Neurosci*. 1989;12(10):366–375.

45. Galvan L, André VM, Wang EA, Cepeda C, Levine MS. Functional differences between direct and indirect striatal output pathways in Huntington's disease. *J Huntingtons Dis*. 2012;1(1):17–25.

46. Sebastianutto I, Cenci MA, Fieblinger T. Alterations of striatal indirect pathway neurons precede motor deficits in two mouse models of Huntington's disease. *Neurobiol Dis*. 2017;105:117–131.

47. Crook ZR, Housman DE. Dysregulation of dopamine receptor D2 as a sensitive measure for Huntington disease pathology in model mice. *Proc Natl Acad Sci U S A*. 2012;109(19):7487–7492.

48. van Deijk A-LF, Camargo N, Timmerman J, et al. Astrocyte lipid metabolism is critical for synapse development and function *in vivo*. *Glia*. 2017;65(4):670–682.

49. Ferris HA, Perry RJ, Moreira GV, et al. Loss of astrocyte cholesterol synthesis disrupts neuronal function and alters whole-body metabolism. *Proc Natl Acad Sci U S A*. 2017;114(5):1189–1194.

50. Santello M, Toni N, Volterra A. Astrocyte function from information processing to cognition and cognitive impairment. *Nat Neurosci*. 2019;22(2):154–166.

51. Boisvert MM, Erikson GA, Shokhirev MN, Allen NJ. The aging astrocyte transcriptome from multiple regions of the mouse brain. *Cell Rep*. 2018;22(1):269–285.

52. Allen NJ, Lyons DA. system formation and function. *Science*. 2018;362(6411):181–185.

53. Linetti A, Fratangeli A, Taverna E, et al. Cholesterol reduction impairs exocytosis of synaptic vesicles. *J Cell Sci*. 2010;123(Pt 4):595–605.

54. Thiele C, Hannah MJ, Fahrenholz F, Huttner WB. Cholesterol binds to synaptophysin and is required for biogenesis of synaptic vesicles. *Nat Cell Biol*. 2000;2(1):42–49.

55. Zhao L, Chen X-J, Zhu J, et al. Lanosterol reverses protein aggregation in cataracts. *Nature*. 2015;523(7562):607–611.

56. Upadhyay A, Amanullah A, Mishra R, Kumar A, Mishra A. Lanosterol suppresses the aggregation and cytotoxicity of misfolded proteins linked with neurodegenerative diseases. *Mol Neurobiol*. 2018;55(2):1169–1182.

57. Lim KL, Ng XH, Grace LGY, Yao TP. Mitochondrial dynamics and Parkinson's disease: Focus on parkin. *Antioxid Redox Signal*. 2012;16(9):935–949.

58. Kacher R, Lamazière A, Heck N, et al. CYP46A1 gene therapy deciphers the role of brain cholesterol metabolism in Huntington's disease. *Brain*. 2019;142(8):2432–2450.

59. Andrews TC, Weeks RA, Turjanski N, et al. Huntington's disease progression. PET and clinical observations. *Brain*. 1999;122(12):2353–2363.

60. Weeks RA, Piccini P, Harding AE, Brooks DJ. Striatal D1 and D2 dopamine receptor loss in asymptomatic mutation carriers of Huntington's disease. *Ann Neurol*. 1996;40(1):49–54.

61. Glass M, Dragunow M, Faull RLM. The pattern of neurodegeneration in Huntington's disease: A comparative study of cannabinoid, dopamine, adenosine and GABA(A) receptor alterations in the human basal ganglia in Huntington's disease. *Neuroscience*. 2000;97(3):505–519.

62. Feigin A, Tang C, Ma Y, et al. Thalamic metabolism and symptom onset in preclinical Huntington's disease. *Brain*. 2007;130(11):2858–2867.

63. van Oostrom JCH, Dekker M, Willemsen ATM, et al. Changes in striatal dopamine D2 receptor binding in pre-clinical Huntington's disease. *Eur J Neurol*. 2009;16(2):226–231.

64. Cha JH, Kosinski CM, Kerner JA, et al. Altered brain neurotransmitter receptors in transgenic mice expressing a portion of an abnormal human Huntington disease gene. *Proc Natl Acad Sci U S A*. 1998;95(11):6480–6485.

65. Ariano MA, Aronin N, Difiglia M, et al. Striatal neurochemical changes in transgenic models of Huntington's disease. *J Neurosci Res*. 2002;68(6):716–729.

66. Backman L, Farde L. Dopamine and cognitive functioning: Brain imaging findings in Huntington's disease and normal aging. *Scand J Psychol*. 2001;42(3):287–296.

67. Martín R, Bajo-Grañeras R, Moratalla R, Perea G, Araque A. Circuit-specific signaling in astrocyte-neuron networks in basal ganglia pathways. *Science*. 2015;349(6249):730–734.

68. Octeau JC, Chai H, Jiang R, et al. An optical neuron-astrocyte proximity assay at synaptic distance scales. *Neuron*. 2018;98(1):49–66.

69. Boussicault L, Alves S, Lamazière A, et al. CYP46A1, the rate-limiting enzyme for cholesterol degradation, is neuroprotective in Huntington's disease. *Brain*. 2016;139(Pt 3):953–970.

70. Araque A, Carmignoto G, Haydon PG, et al. Gliotransmitters travel in time and space. *Neuron*. 2014;81(4):728–739.

71. Khakh BS, Beaumont V, Cachope R, et al. Unravelling and exploiting astrocyte dysfunction in Huntington's disease. *Trends Neurosci*. 2017;40(7):422–437.

72. Covelo A, Araque A. Neuronal activity determines distinct gliotransmitter release from a single astrocyte. *Elife*. 2018;7:e32237.